ACS APPLIED MATERIALS & INTERFACES

Research Article

www.acsami.org

Manganese-Loaded Dual-Mesoporous Silica Spheres for Efficient T1- and T2-Weighted Dual Mode Magnetic Resonance Imaging

Dechao Niu,[†] Xiaofeng Luo,[†] Yongsheng Li,*[,†] Xiaohang Liu,[‡] Xia Wang,[§] and Jianlin Shi*[,†,§]

[†]Lab of Low-Dimensional Materials Chemistry, Key Laboratory for Ultrafine Materials of Ministry of Education, School of Materials Science and Engineering, East China University of Science and Technology, Shanghai 200237, P. R. China

[‡]Department of Radiology, Shanghai Cancer Hospital, Fudan University, Shanghai, 200032, P. R. China

[§]State Key Laboratory of High Performance Ceramics and Superfine Microstructure, Shanghai Institute of Ceramics, Chinese Academy of Sciences, Shanghai 200050, P. R. China

Supporting Information

ABSTRACT: A novel class of manganese-based dual-mode contrast agents (DMCAs) based on the core−shell structured manganese-loaded dual-mesoporous silica spheres (Mn-DMSSs) for simultaneous T1- and T2-weighted magnetic resonance imaging (MRI) has been successfully reported. The in vitro MR tests demonstrate that the Mn-based DMCAs display an excellent simultaneous T1-weighted and T2-weighted MR imaging effect with a noticeably high T1 relaxivity (r_1) of 10.1 $mM^{-1}s^{-1}$ and a moderately high T2 relaxivity (r_2) of 169.7 $mM^{-1}s^{-1}$. The Mn-based DMCAs exhibit negligible cytotoxicity with >80% cell viability at a concentration of up to 200 μg/mL in human liver carcinoma (HepG2) and mouse macrophage (RAW264.7) cells after 24 h. Confocal laser scanning microscopy (CLSM) results show that the Mn-DMSSs were internalized via endocytosis and located in the cytoplasm but not in the nucleus. The in vivo experiment shows that the signals of rat liver increased by 29% under T1-weighted imaging mode and decreased by 28% under T2-weighted imaging mode in 5 min postinjection of Mn-DMSSs, which reveal that the novel Mn-loaded DMSSs can be used as both positive (T1-weighted) and negative (T2-weighted) MR contrast agents in further biomedical applications.

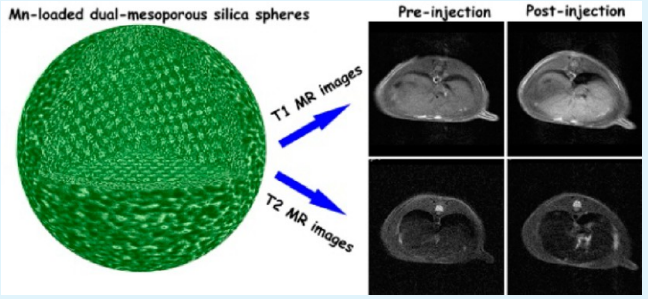

KEYWORDS: *manganese, dual-mesoporous, dual-mode, magnetic resonance imaging*

1. INTRODUCTION

Various imaging techniques including magnetic resonance imaging (MRI), computed tomography (CT), positron emission tomography (PET), and optical microscopy in the bioimaging fields, have been widely employed to increase the accuracy of disease diagnosis, especially for cancer.[1−3] Among these imaging methods, MRI is believed to be one of the most powerful diagnostic tools due to its inherent advantages such as noninvasiveness, safety, and high spatial resolution.[4] In most cases of clinical application, MR contrast agents are applied to enhance the contrast, which in a way increases the sensitivity and the quality of the images for more accurate diagnosis.[5] Generally, MR contrast agents are divided into two categories: one is paramagnetic complexes of gadolinium or manganese ions, which can induce the local relaxation change of the nearby water protons and mainly reduce longitudinal (T1) relaxation time, providing positive contrast (bright signal) on the T1-weighted MR image; the other is superparamagnetic, mostly iron oxide-based, nanoparticles, which can shorten transverse (T2) relaxation time, providing negative contrast (dark signal) on the T2-weighted MR image. Up to now, different types of MR contrast agents including Gd-based complexes or nanoparticles[6−9] and manganese oxide nanoparticles[10−13] for T1-weighted imaging or iron oxide-based nanoparticles[14−17] for T2-weighted imaging have been designed and synthesized. However, each mode contrast agent has its own unique advantages and limitations. For example, some clinical Gd-based contrast agents may result in potential danger such as nephrogenic systemic fibrosis (NSF) for patients with severe renal disease or following liver transplant, as claimed by the Food and Drug Administration (FDA) organization since 2006.[18] On the other hand, the clinical applications of iron-oxide based contrast agents are quite limited because of magnetic susceptibility artifacts and their negative contrast effect, which may not be clearly distinguishable from the low-level MR signal arising from adjacent tissues such as bone or vasculature.[19,20]

Recently, there are several reports on the design and synthesis of dual-mode contrast agents (DMCAs) by the combination of two different modes of imaging (T1- and T2-

Received: May 16, 2013
Accepted: September 20, 2013
Published: September 20, 2013

weighted MR imaging) in order to improve the diagnosis accuracy of diseases.[21−27] The greatest advantage of the dual imaging strategies is that two complementary images can be provided simultaneously by employing a single instrumental system, compared with other bimodal imaging technologies (e.g., MR/optical), which need to consider the different penetration depths and spatial/time resolutions of multiple imaging devices. Unfortunately, most of the reported DMCAs usually consisted of two kinds of functional species: one is commonly Gd- or Mn-based materials for T1-weighted MR imaging; the other is Fe-based nanoparticles for T2-weighted MR imaging. Due to the inevitable severe interference between these two different contrast agents,[22,24,25] it is difficult to develop high quality DMCAs with simultaneously high T1 relaxivity and T2 relaxivity. Thus, developing a class of novel DMCAs with single component (Fe-, Mn-, and Gd-based) without conflicting effects between the two kinds of functional units is still a great challenge. Recently, although a new class of iron-based DMCAs has been developed by employing ultrasmall iron oxide (∼3 nm in diameter) as a functional unit, their T2 relaxivities (r_2) are low due to the smaller size of iron oxide nanoparticles.[28−31]

Among these functional species, the manganese element is a required trace mineral for all known living organisms. However, it can lead to a poisoning syndrome in mammals with neurological damage, hepatic failure, and cardiac toxicity as larger amounts of manganese are used.[32] For manganese-based MR contrast agents, one effective method to reduce the side effect is to increase the relaxivity of CAs to enhance the contrast effect, resulting in the greatly lowered dosage. Recently, manganese-based nanoparticulate systems, such as MnO, silica-coated MnO, and hollow MnO nanoparticles have been used as a new class of T1-weighted MR contrast agents.[10−13] Unfortunately, the longitudinal relaxivity (r_1) of these nanoparticles was still very low, which was largely due to the enhanced shielding effect between the paramagnetic centers in the nanocrystal lattices and water molecules resulting from the larger particle sizes (>5 nm). Moreover, these results have demonstrated that both longitudinal relaxivity (r_1) and transversal relaxivity (r_2) were increased with the size of the nanoparticles decreasing. Therefore, the key issue to design high quality manganese-based DMCAs with simultaneously high r_1 and r_2 values to date is the adjustment of particle diameter of manganese oxide. In this Article, we report a novel class of manganese-based DMCAs based on the core−shell structured manganese-loaded dual-mesoporous silica spheres (designated as Mn-DMSSs) for simultaneous T1- and T2-weighted MR imaging. The Mn-DMSSs were synthesized by utilizing an amphiphilic block copolymer (polystyrene-*b*-poly (acrylic acid), PS-*b*-PAA) and cetyltrimethyl ammonium bromide (CTAB) as dual-templates and a subsequent oxidation−reduction reaction. The in vitro and in vivo MR results show that Mn-DMSSs displayed excellent contrast effects in both T1- and T2-weighted MR imaging.

2. EXPERIMENTAL SECTION

2.1. Chemicals. Tetraethyl orthosilicate (TEOS, AR), potassium permanganate ($KMnO_4$, ≥99.5%), ammonia solution (25−28%), and cetyltrimethyl ammonium bromide (CTAB, ≥99%) were purchased from Shanghai Lingfeng Chemical Reagent Co. Ltd. Tetrahydrofuran (THF, AR) and ethanol (AR) were purchased from Sinopharm Chemical Reagent Co. LTD (Shanghai, China). The pure water with a resistivity of 18.2 MΩ·cm was used in all of experiments. All of the reagents were used without further purification.

2.2. Synthesis of PS-*b*-PAA. Amphiphilic block copolymer, polystyrene-*b*-poly (acrylic acid) (PS-*b*-PAA), was synthesized via sequential atomic transfer radical polymerization (ATRP) as previously reported.[33]

2.3. Synthesis of DMSSs. Dual-mesoporous silica spheres were prepared through a reported method with slight modification.[34] In a typical synthesis, 50 mg of PS_{100}-*b*-PAA_{16} was first dissolved in 10 mL of THF to form the organic solution. Then, the above oil solution was poured into a mixture solution containing 40 mL of H_2O, 65 mg of CTAB, and 1.5 mL of ammonia. After stirring for 10 min, the mixture oil−water solution was diluted with 80 mL of ethanol. After stirring for 120 min, 0.3 g of TEOS dissolved in 5 mL of ethanol was added dropwise to the oil−water solution with continuous stirring. After reaction for 18 h at room temperature, the sample was collected by centrifugation (10 000 r/min, 15 min) and washed with pure water several times. The purified sample was dried in the oven and further calcined at 500 °C for 6 h in order to remove the surfactants (CTAB and PS-*b*-PAA).

2.4. Synthesis of Mn-DMSSs. The load of manganese oxide was achieved by the oxidation−reduction reaction between $KMnO_4$ and organic surfactant according to the literature reported previously.[35,36] Briefly, a certain amount of $KMnO_4$ was added into the 30 mL of the manganese oxide loading dual-mesoporous silica spheres aqueous solution without removal of surfactants under magnetic stirring. The mixture solution was transferred into a water bath (40 °C), and the reaction was continued for 4 h; then, the sample was collected by centrifugation and washed with pure water several times to remove unreacted species. After the sample was dried at 100 °C, the organic surfactants were removed by calcination in air at 500 °C for 6 h. Finally, the sample was heated in mixed H_2 (5% volume percentage) and N_2 (95% volume percentage) gases at 400 °C for 2 h.

2.5. In Vitro MRI. The in vitro MR imaging experiment was performed on a 3.0 T clinical MRI instrument (GE Signa HDx 3.0 T). For the T2-weighted fast-recovery fast spin−echo (FR-FSE) sequence, the following parameters were adopted: TR (repetition time) = 2000 ms, TE (echo time) = 106 ms, field of view (FOV) = 16 ms, slice thickness = 3.0 mm, echo length = 15, matrix = 192 × 128, and number of acquisitions = 2. For the T1-weighted fast spin−echo (FSE) sequence, the following parameters were used: TR = 1000 ms, TE = 7.8 ms, field of view (FOV) = 16 ms, slice thickness = 3.0 mm, echo length = 15, matrix = 128 × 128, and number of acquisitions = 2. For MRI tests, the Mn content of the Mn-DMSSs in water was determined by inductively coupled plasma atomic emission spectrometry (ICP-AES).

2.6. T2 Relaxivity Measurement. Solutions of Mn-DMSSs containing Mn at various concentrations were prepared in pure water. MR T2 mapping experiments to obtain T2 relaxation time were performed by using a spin−echo (SE) sequence with a 3.0 T clinical MRI instrument (GE Signa HDx 3.0 T) with the following parameters: TR = 4000 ms; TE = 13, 26, 39, and 52 ms. Relaxivity values of r_2 were calculated through the curve fitting of 1/T2 relaxation time (s^{-1}) versus the Mn concentration (mM).

2.7. T1 Relaxivity Measurement. Solution of Mn-DMSSs containing Mn at various concentrations were prepared in pure water. MR T1 mapping experiments to obtain T1 relaxation time were performed by using FSE sequence with the following parameters: TR = 1000, 2000, 3000, and 4000 ms; TE = 7.8 ms. Relaxivity values of r_1 were calculated through the curve fitting of 1/T1 relaxation time (s^{-1}) versus the Mn concentration (mM).

2.8. In Vitro Cytotoxicity and Cellular Uptake. The in vitro toxic effects of Mn-DMSSs were studied using two kinds of cell lines (HepG2 and RAW 264.7). These two cell lines were cultured in Dulbecco's Modified Eagle's medium (DMEM) containing 10% fetal bovine serum. Cells seeded in 96-well plates were cultured for 24 h and then treated with the nanoparticles concentrations (from 10 to 400 μg per well) dissolved in the corresponding culture medium containing 10% fetal bovine serum for 24 h. The cytotoxicity was evaluated using the MTT conversion test. Briefly, 100 μL of MTT

Scheme 1. Formation Process of Mn-DMSSs[a]

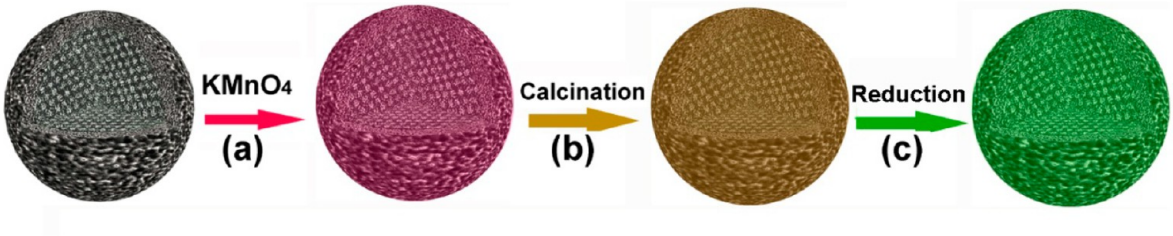

[a](a) Template oxidation by $KMnO_4$ resulting in the simultaneous introduction of manganese species; (b) calcination to remove residue organic template; (c) reduction of manganese ions to Mn^{2+} for enhanced MR imaging ability.

solution was added to each well. After incubation for 4 h, each well was treated with 100 μL of DMSO with pipetting for 5 min. After the incubation period, the optical density was measured at 490 nm. Each result was the average of eight wells, and 100% viability was determined from untreated cells.

To observe cellular uptake of Mn-DMSSs, 1×10^4 HepG2 cells per well were cultured in an 8% well chamber slide (Nalgen Nunc, Naperville, IL) and incubated with Mn-DMSSs at 100 μg/mL. After 4 and 24 h, the cells were washed with phosphate buffered saline (PBS), fixed with 4% paraformaldehyde, and stained with 4′,6-diamidino-2-phenylindole (DAPI, 1 Eg/mL in PBS, Roche). The fluorescence images were acquired by confocal laser scanning microscopy (CLSM) (LSM 510 META, Carl Zeiss, Germany).

2.9. In Vivo MRI. In vivo MR imaging was performed with Sprague–Dawley (SD) rats (female, weight ~200 g). All animal procedures were in agreement with the guidelines of the Instituonal Animal Care and Use Committee. Briefly, MR images were taken prior to injection of nanoparticles and at appropriate intervals postinjection. Mn-DMSSs were injected through the tail vein at a dose of 0.8 mg Mn/kg (measured by ICP-AES). Then, the rat was taken for the MRI test. MRI was performed using a 3.0 T clinical MRI instrument (GE Signa HDx 3.0 T) with a fast spin–echo sequence (TR/TE = 2000/19 ms (T2), TR/TE = 85/3.5 ms (T1), flip-angle = 90°, echo length = 10, field of view = 16 cm, slice thickness = 2 mm, matrix = 512 × 512). All MRI quantitative analyses were carried out by one radiologist. Signal intensities (SIs) were measured in defined regions of interest (ROI), which were in comparable locations within tumor sites. Relative signal changed values were calculated using SI measurements before (SI_{pre}) and after (SI_{post}) injection of contrast agents, using the formula: $[(SI_{post} - SI_{pre})/SI_{pre}] \times 100$; SI_{post} values were collected at 5 and 15 min. The standard deviation of signal intensity is derived from a group of the ROI (n = 3).

2.10. Characterization. TEM (transmission electron microscopy) analysis was conducted on a JEM 2100F electron microscope operated at 200 kV. The specimens of TEM were prepared by dropping the sample onto a copper mesh coated with an amorphous carbon film. This mesh was then dried in air. FESEM (field emission scanning electron microscopy) analysis was conducted on an JEOL JSM6700F electron microscope. N_2 adsorption and desorption isotherms were measured using Quantachrome NOVA 4200e. The specific surface area and the pore size distribution were calculated by using the Brunauer–Emmett–Teller (BET) and Barrett–Joyner–Halenda (BJH) methods, respectively. The mean diameter of the samples was measured by dynamic light scattering using a Zeta potential/particle Sizer Nicomp TM 380 ZLS (PSS Nicomp particle size system, U.S.A.). The X-ray powder diffraction patterns were recorded on a BRUKER-AXS diffractometer (Bruker, Germany) using Cu Kα radiation (λ = 0.1542 nm). X-ray photoelectron spectroscopy (XPS) experiments were performed on ESCALAB 250Xi (Thermo Scientific).

3. RESULTS AND DISCUSSION

The formation process of Mn-DMSSs is illustrated in Scheme 1. First, in step a, core–shell structured dual-mesoporous silica spheres without removing the templates were synthesized according to our previously reported approach.[34] In order to encapsulate manganese, potassium permanganate ($KMnO_4$), a highly oxidative agent, was used to oxidize the organic templates (e.g., CTAB) in situ by a simple oxidation–reduction reaction,[35,36] resulting in the formation of the Mn-DMSSs. After the calcination (500 °C, 6 h) to remove the residual organic templates (step b), the manganese-loaded dual-mesoporous silica spheres were treated in H_2/N_2 atmosphere (400 °C, 2 h), which is favorable for improving the T1-weighted MR contrast effects (step c).[37]

Representative transmission electron microscopy (TEM) images of DMSSs and Mn-DMSSs are shown in Figure 1a,b. It can be clearly seen that well-defined core–shell structured dual-mesoporous silica nanospheres, which have smaller pores in the shell and ordered larger pores in the core, have been obtained by employing two different kinds of templates (PS-*b*-PAA and CTAB). After loading of manganese species, the spherical particle morphology and core–shell structure of Mn-DMSSs did not show visible changes, as shown in Figure 1b. Moreover, the dual-mesoporous structure of Mn-DMSSs was also confirmed by the N_2 sorption results (see Supporting Information, Figure S1). The specific surface area and total volume of Mn-DMSSs were calculated to be 679 m^2/g and 1.8 cm^3/g, respectively. In addition, two sets of mesopores at 2.1 and 18.9 nm in diameter have been obtained as can be identified from the corresponding distribution curve of Mn-DMSSs, which was obtained by the Barrett–Joyner–Halenda (BJH) method. The hydrodynamic diameter of Mn-DMSSs determined by dynamic light scattering (DLS) is 199 nm, demonstrating that they are monodispersed and do not aggregate in water (see Supporting Information, Figure S2). Noticeably, manganese oxide nanoclusters could not be identified in the TEM images due to their small sizes (<2 nm) and high dispersity in the silica matrix, as evidenced from the wide-angle XRD pattern of Mn-DMSSs (see Supporting Information, Figure S3). In order to confirm the presence of manganese species in the dual-mesoporous silica spheres, the energy-dispersive X-ray spectroscopy (EDS) line scanning and corresponding elemental mapping analysis were conducted, as shown in Figure 1c. It is showed that manganese elements were mainly located in the shell region, i.e., small pore channels of DMSSs. It is concluded that the manganese species could be introduced successfully into the pores of DMSSs by adopting the simple oxidation–reduction approach. In addition, the valence state of Mn element in Mn-DMSSs has been characterized by XPS analysis. As shown in the Supporting Information, Figure S4, the Mn $2p_{1/2}$ and $2p_{3/2}$ of Mn-DMSSs before H_2 reduction are mainly located at 654.2 and 642.5 eV,

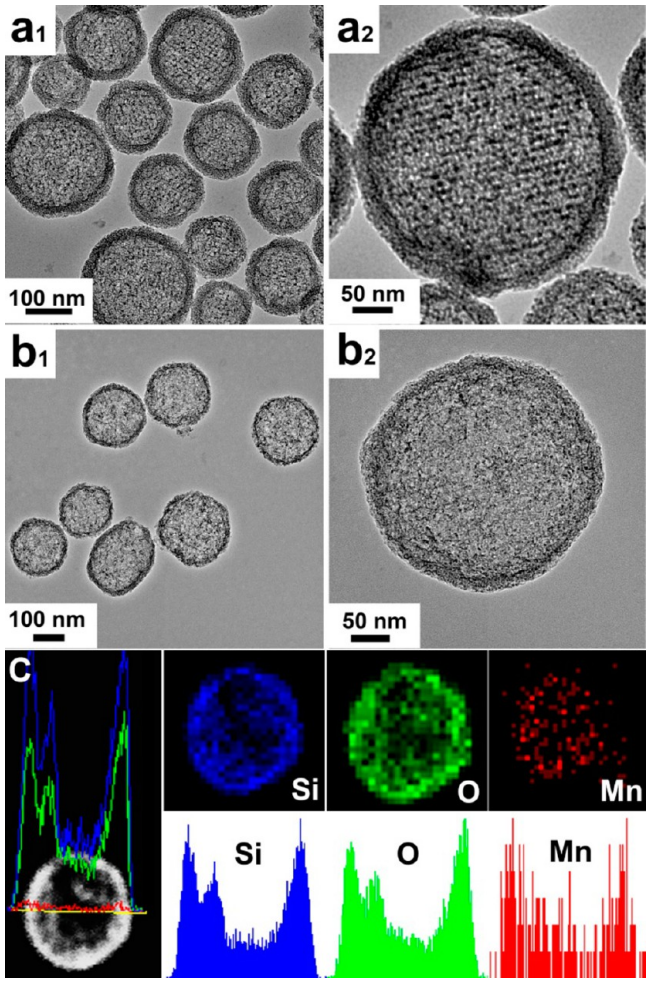

Figure 1. TEM images of DMSSs (a_1, a_2) and Mn-DMSSs (b_1, b_2). (c) Scanning TEM image with high angle annular dark field (STEM-HAADF) and corresponding EDS elemental mapping images and EDS line profiles of Mn-DMSSs.

respectively. These values are in good agreement with literature values of Mn^{4+} in MnO_2.[38] After reduction, the $2p_{3/2}$ of Mn-DMSSs shifts toward a lower binding energy of 641.4 eV, which is in correspondence with the binding energy of Mn^{2+} in MnO.[39] On the basis of these results, it is demonstrated that the phase of manganese species in the pores of DMSSs might be transformed from MnO_2 to MnO under the reduction condition.

In order to investigate the application potentials in MR imaging, the dual mode (T1 and T2) contrast effects of Mn-DMSSs were measured using a clinical 3.0 T MRI scanner. As shown in the insets of Figure 2, the brighter signals in T1-weighted images and the darker signals in T2-weighted images can be observed at increased Mn concentrations. To quantitatively evaluate the MR contrast enhancements, the longitudinal (r_1) and transverse (r_2) relaxivity values were calculated through the curve fitting of relaxation time versus the metal concentration (Figure 2a,b). The results show that the r_1 and r_2 values of Mn-DMSSs are 10.1 and 169.7 $mM^{-1}s^{-1}$, respectively, which are considerably higher than those of most other kinds of reported dual mode MR contrast agents consisting of various components (see Supporting Information, Table S1). Further calculation shows that Mn-DMSSs possesses an extremely high Mn^{2+} ions payload (approximately 9.14 × 10^7) with particle relaxivities estimated to be r_1 = 9.23 × 10^8 and r_2 = 1.55 × 10^{10} $mM^{-1}s^{-1}$ (see Supporting Information, Table S2). Moreover, the values (r_1 and r_2) are comparable to that of the conventional T1-weighted contrast agent, Gd-DTPA (gadolinium-diethylenetriaminepentaacetate, Magnevist, r_1 = 9.6 $mM^{-1}s^{-1}$ at 3.0 T), and the well-known iron oxide-based T2-weighted contrast agent, Feridex (r_2 = 108 $mM^{-1}S^{-1}$ at 3.0 T),[24] indicating that Mn-DMSSs can act as both T1- and T2-weighted MR contrast agents.

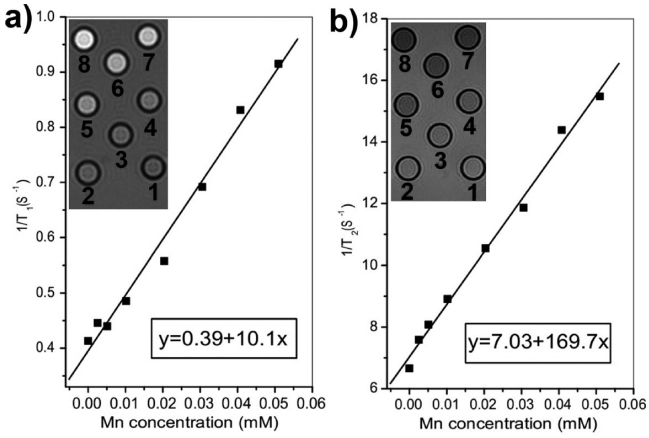

Figure 2. (a) Longitudinal (1/T1) and (b) transverse (1/T2) relaxation rates of aqueous solutions of Mn-DMSSs. (The insets are T1-weighted and T2-weighted MR images of Mn-DMSSs with increased Mn concentrations 1−8: 0, 0.0025, 0.0051, 0.010, 0.020, 0.031, 0.041, and 0.051 mM.) The experimental data was obtained on a 3.0 T MRI scanner.

In the present work, the high r_1 value of Mn-DMSSs can be attributed to the following three factors: the first is that much lower $KMnO_4$ concentration (2 mM) was employed to oxidize the CTAB molecules compared to the previously reported work,[37] resulting in the formation of ultrasmall manganese oxide nanoclusters highly dispersed in the pores of the DMSSs. To test the hypothesis, we employed Mn-DMSSs prepared with higher $KMnO_4$ concentrations of 10 and 50 mM as two control samples. The morphologies, diameters, and pore structures of these samples were also analyzed by TEM, DLS, and N_2 sorption techniques (see Supporting Information, Figures S5, S6, and S7). By comparison (see Supporting Information, Table S3 and Figure S8), it can be concluded that the r_1 value decreases at increased $KMnO_4$ concentration, further demonstrating that the utilization of low concentration $KMnO_4$ is favorable for the enhancement of T1-weighted contrast effect. Moreover, when a very high concentration of $KMnO_4$ (50 mM) was used, the spherical morphology was destroyed and the smaller pores in the shell also disappeared (see Supporting Information, Figures S6 and S7). Second, more Mn^{2+} ions were produced through calcination in a reducing environment, which can intensify the T1-weighted MR imaging as reported previously.[37] Third, the unique dual-mesoporous structure of Mn-DMSSs could increase the diffusion rate of water molecules inside the mesopores, further enhancing the r_1 relaxivity.[40]

For the high r_2 value of Mn-DMSSs, the enhanced T2-weighted contrast effect of Mn-DMSSs may be attributed to the T2 relaxivity time shortening by ultrasmall manganese oxide nanoclusters (<2 nm) in DMSSs. Compared with larger MnO nanoparticles (>5 nm),[10] ultrasmall manganese oxide nanoclusters with higher surface-to-volume ratio exhibit a larger proportion of noncompensated surface spins on the anti-

ferromagnetic core and higher magnetization values, which may cause the shorter T2 relaxation time and thereafter the higher r_2 value, which is in accordance with the previous work.[41] Besides, the samples with smaller size were synthesized by using the same $KMnO_4$ concentration (2 mM) as a control, and the corresponding MR relaxivities were tested (see Supporting Information, Figure S9 and S10) for a better understanding the mechanism of the T2 effect of Mn-DMSSs. The r_2 value was calculated to be 166.9 $mM^{-1}s^{-1}$, which is similar to that of Mn-DMSSs with average size of 200 nm. It indicates that the increased r_2 is independent of the size of the whole particles. The detailed mechanism on the excellent T2 effect of Mn-DMSSs is still under investigation, and additional analysis is needed in our further work.

The cytotoxicity of Mn-DMSSs was evaluated by choosing two typical kinds of cell lines (human liver carcinoma cell HepG2 and mouse macrophage cell RAW264.7). The MTT assay (see Supporting Information, Figure S11) revealed that no apparent toxic effects of Mn-DMSSs were observed in 24 h of incubation at a lower concentration (<200 $\mu g \cdot mL^{-1}$ or 5 μg $Mn \cdot mL^{-1}$), but relatively low cell viabilities below 80% were found with a large dose of nanoparticles in both normal cells (RAW264.7) and cancer cells (HepG2). The possible reason for the slight toxicity of Mn-DMSSs may be attributed to the release of excess Mn ions from the acidic environment (e.g., endosomes or lysosomes of cells), which is similar with other literature reported previously.[32] In order to confirm the hypothesis, the release curves of Mn ions from the Mn-DMSSs in phosphate-buffered saline (PBS) solutions of various pH values (7.2 and 5.5) have been tested. As shown in the Supporting Information, Figure S12, only 4% manganese ions were released from the Mn-DMSSs at pH values of 7.2 within 48 h. In contrast, 20% manganese ions were found leached out from the spheres at pH 5.5. These results indicate that the structure of Mn-DMSSs was stable at neutral environment. More importantly, this pH-responsive property would be very helpful for MRI contrast agents as pH values varied in different tissues and cellular compartments. For example, the pH value of tumor extracellular is about 6.5, while in endosomes and lysosomes of cells, it is ca. 5.0−5.5.[42,43]

In addition, to investigate the cellular uptake of Mn-DMSSs, fluorescein isothiocyanate (FITC) was grafted on the surface of Mn-DMSSs and then observed by confocal laser scanning microscopy (CLSM). As shown in Figure 3, it was found that FITC-labeled Mn-DMSSs at a concentration of 100 $\mu g \cdot mL^{-1}$ could be efficiently endocytosized by HepG2 cells. In detail, at 4 h incubation, only spot-like green fluorescence can be observed in the CLSM images (Figure 3a−d), demonstrating that a small amount of Mn-DMSSs was internalized and most of the nanoparticles were located in the membrane region. In a prolonged time period (24 h), higher fluorescent intensity was observed in the cytoplasm, implying that more particles were located in the inside of cells. No fluorescent signals are seen in the nuclei, indicating that Mn-DMSSs could not pass through the nuclear membrane (Figure 3e−h). In addition to the time periods, the effect of particle concentration on the cell uptake has been investigated (see Supporting Information, Figure S13). The results show that more particles were found accumulated within the cytoplasm and cell membrane of HepG2 cells as higher particle concentrations were used (200 and 400 $\mu g \cdot mL^{-1}$). On the basis of the above analysis, it is concluded that both the time- and dose-dependent uptake mechanisms influence the cell uptake process.

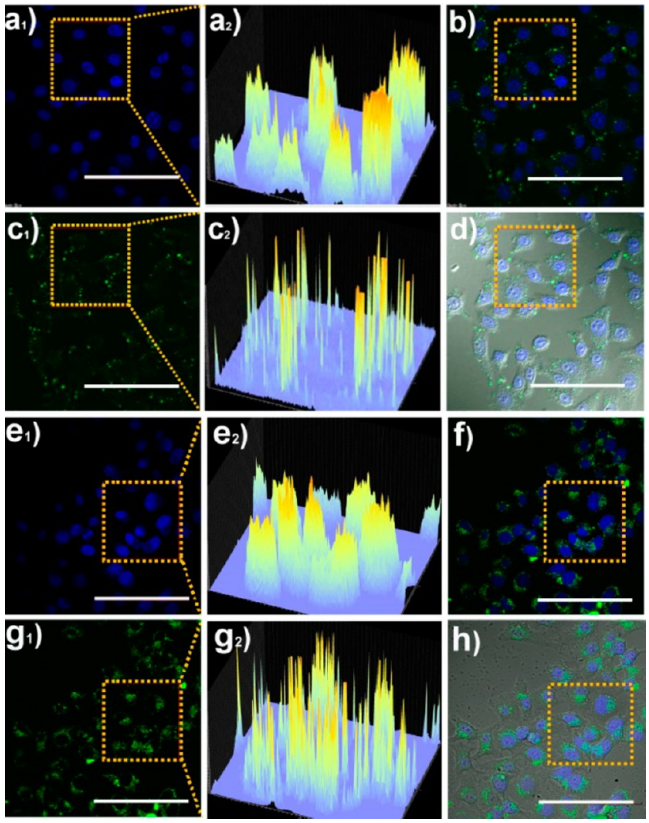

Figure 3. Confocal laser scanning microscopic (CLSM) images of HepG2 cells incubated with FITC-labeled Mn-DMSSs at a concentration of 100 $\mu g/mL$ for 4 h (a−d) and 24 h (e−h). (a_1, a_2; e_1, e_2) The cell nuclei stained with blue 4′,6-diamidino-2-phenylindole (DAPI) and the corresponding enlarged two-dimensional fluorescent intensity image. (b, f) Merged image of blue (DAPI) and green (FITC-labeled Mn-DMSSs). (c_1, c_2; g_1, g_2) The green fluorescence of FITC and the corresponding enlarged two-dimensional fluorescent intensity image. (d, h) Merged image of blue (DAPI), green (FITC-labeled Mn-DMSSs), and differential interference contrast (DIC). The scale bar is 100 μm.

The in vivo MRI experiments were performed to further demonstrate the dual mode contrast effects of Mn-DMSSs using a SD rat as a model. As shown in Figure 4a, we acquired the T1- and T2-weighted MR images sequentially before and after the intravenous injection of Mn-DMSSs, with a dose of 0.5 mg Mn kg^{-1} of rat body weight. Compared with the preinjection images, a significantly brightened signal in T1-weighted MR images and a clearly darkened signal in T2-weighted MR images can be found in the liver at the 5 min postadministration, owing to the heavy accumulation of nanoparticles in the mononuclear phagocyte system (MPS), especially the Kupffer cells in the liver.[44,45] Through quantitative analysis, the MR signal intensity changes are approximately 28% and 29% in T1 and T2 imaging in the liver region, respectively (Figure 4b). These results show that the novel manganese-loaded DMSSs have unique dual mode MR imaging capability to simultaneously show excellent T1- and T2-weighted contrast enhancement in vivo, which can provide more comprehensive imaging information and higher diagnostic accuracy, particularly in the detection and diagnosis of lesions in the liver.

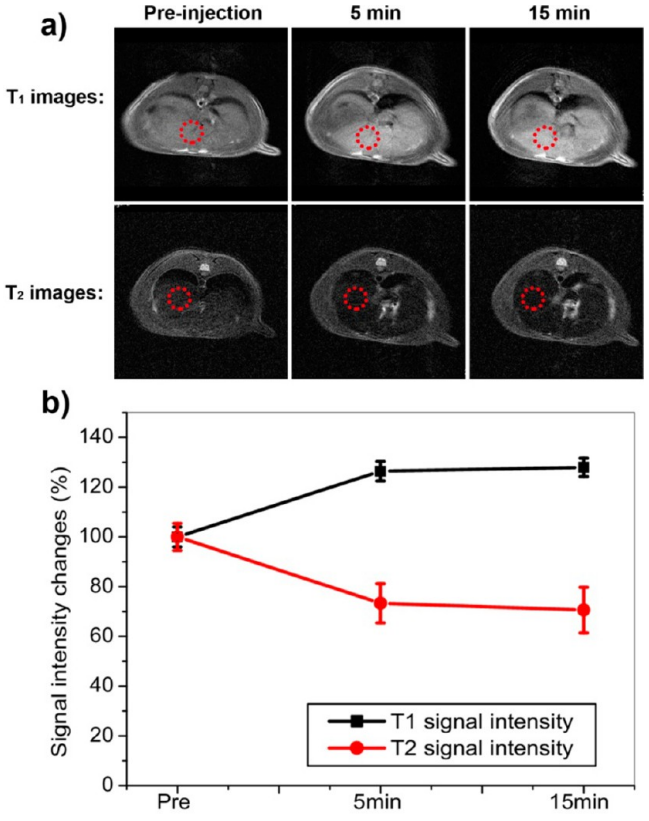

Figure 4. Simultaneous T1 and T2 imaging of a SD rat liver on a 3.0 T MRI scanner. (a) In vivo T1- and T2-weighted MR images and (b) the corresponding signal intensity of SD rat liver before and after intravenous injection of Mn-DMSSs nanoparticles with a dose of 0.5 mg Mn kg^{-1} at different time points (5 and 15 min). The standard deviation of signal intensity is derived from a group of the ROI (n = 3).

4. CONCLUSIONS

In conclusion, a new class of Mn-based DMCAs (Mn-DMSSs) has been developed by embedding ultrasmall manganese oxide nanoclusters in the pore channels of DMSSs using a simple oxidation−reduction reaction. The nanosized Mn-DMSSs show an average diameter of 199 nm, unique dual-mesoporous nanostructure, and satisfactory dispersity in aqueous solution. The in vitro MR tests demonstrate that the Mn-based DMCAs display an excellent simultaneous T1-weighted and T2-weighted MR imaging effect with a noticeably high T1 relaxivity (r_1) of 10.1 $mM^{-1}s^{-1}$ and a moderately high T2 relaxivity (r_2) of 169.7 $mM^{-1}s^{-1}$, which are comparable to those obtained by using commercial Gd-based T1-type contrast agent and clinical iron oxide-based T2-type contrast agent, respectively. The in vivo experiment shows that the signals of liver increased by 29% under T1-weighted imaging mode and decreased by 28% under T2-weighted imaging mode in 5 min postinjection of Mn-DMSSs, which is attributed to the phagocytosis by the RES. Therefore, these kinds of Mn-loaded DMSSs could be used as excellent dual mode MR contrast agents for the diagnosis of diseases in further biomedical applications.

■ ASSOCIATED CONTENT

Ⓢ Supporting Information

Nitrogen-sorption isotherms and BJH pore-size distributions of DMSSs and Mn-DMSSs; hydrodynamic diameter, wide-angle XRD pattern, and in vitro cytotoxicities against HepG2 and RAW264.7 of Mn-DMSSs; TEM images, hydrodynamic diameters, nitrogen-sorption isotherms, BJH pore-size distributions, and MR relaxivities of various Mn-DMSSs prepared using different $KMnO_4$ concentrations. This material is available free of charge via the Internet at http://pubs.acs.org.

■ AUTHOR INFORMATION

Corresponding Authors

*Fax: 86-21-64250740. E-mail: ysli@ecust.edu.cn.
*Fax: 86-21-64250740. E-mail: jlshi@sunm.shcnc.ac.cn.

Author Contributions

The manuscript was written through contributions of all authors. All authors have given approval to the final version of the manuscript.

Notes

The authors declare no competing financial interest.

■ ACKNOWLEDGMENTS

This work was financially supported by the National Basic Research Program of China (973 Program, 2012CB933602); Program for New Century Excellent Talents in University (NCET-10-0379); Scientific Innovation Project of Shanghai Municipal Education Commission (Grant No. 11ZZ53); The National Natural Science Foundation of China (Grant Nos. 51172070, 51132009, and 51202068), and The Fundamental Research Funds for the Central Universities (Grant Nos. WD1114002 and WD1214010).

■ REFERENCES

(1) Janib, S. M.; Moses, A. S.; MacKay, J. A. *Adv. Drug Delivery Rev.* **2010**, *62*, 1052−1063.
(2) Louie, A. Y. *Chem. Rev.* **2010**, *110*, 3146−3195.
(3) Mahmoudi, M.; Serpooshan, V.; Laurent, S. *Nanoscale* **2011**, *3*, 3007−3026.
(4) Terreno, E.; Castelli, D. D.; Viale, A.; Aime, S. *Chem. Rev.* **2010**, *110*, 3019−3042.
(5) Bellin, M. F. *Eur. J. Radiol.* **2006**, *60*, 314−323.
(6) Turner, J. L.; Pan, D. P. J.; Plummer, R.; Chen, Z. Y.; Whittaker, A. K.; Wooley, K. L. *Adv. Funct. Mater.* **2005**, *15*, 1248−1254.
(7) Luo, K.; Liu, G.; She, W. C.; Wang, Q. Y.; Wang, G.; He, B.; Ai, H.; Gong, Q. Y.; Song, B.; Gu, Z. W. *Biomaterials* **2011**, *32*, 7951−7960.
(8) Caravan, P.; Ellison, J. J.; McMurry, T. J.; Lauffer, R. B. *Chem. Rev.* **1999**, *99*, 2293−2352.
(9) Ahren, M.; Selegard, L.; Klasson, A.; Soderlind, F.; Abrikossova, N.; Skoglund, C.; Bengtsson, T.; Engstrom, M.; Kall, P. O.; Uvdal, K. *Langmuir* **2010**, *26*, 5753−5762.
(10) Na, H. B.; Lee, J. H.; An, K. J.; Park, Y. I.; Park, M.; Lee, I. S.; Nam, D. H.; Kim, S. T.; Kim, S. H.; Kim, S. W.; Lim, K. H.; Kim, K. S.; Kim, S. O.; Hyeon, T. *Angew. Chem., Int. Ed.* **2007**, *46*, 5397−5401.
(11) Shin, J. M.; Anisur, R. M.; Ko, M. K.; Im, G. H.; Lee, J. H.; Lee, I. S. *Angew. Chem., Int. Ed.* **2009**, *48*, 321−324.
(12) Lee, Y. C.; Chen, D. Y.; Dodd, S. J.; Bouraoud, N.; Koretsky, A. P.; Krishnan, K. M. *Biomaterials* **2012**, *33*, 3560−3567.
(13) Kim, T.; Momin, E.; Choi, J.; Yuan, K.; Zaidi, H.; Kim, J.; Park, M.; Lee, N.; McMahon, M. T.; Quinones-Hinojosa, A.; Bulte, J. W. M.; Hyeon, T.; Gilad, A. A. *J. Am. Chem. Soc.* **2011**, *133*, 2955−2961.
(14) Corot, C.; Robert, P.; Idee, J. M.; Port, M. *Adv. Drug Delivery Rev.* **2006**, *58*, 1471−1504.
(15) Liu, D. F.; Wu, W.; Ling, J. J.; Wen, S.; Gu, N.; Zhang, X. Z. *Adv. Funct. Mater.* **2011**, *21*, 1498−1504.
(16) Lee, N.; Hyeon, T. *Chem. Soc. Rev.* **2012**, *41*, 2575−2589.
(17) Tanaka, K.; Narita, A.; Kitamura, N.; Uchiyama, W.; Morita, M.; Inubushi, T.; Chujo, Y. *Langmuir* **2010**, *26*, 11759−11762.

(18) Sieber, M. A.; Steger-Hartmann, T.; Lengsfeld, P.; Pietsch, H. *J. Magn. Reson. Imaging* **2009**, *30*, 1268−1276.
(19) Na, H. B.; Song, I. C.; Hyeon, T. *Adv. Mater.* **2009**, *21*, 2133−2148.
(20) Laurent, S.; Forge, D.; Port, M.; Roch, A.; Robic, C.; Elst, L. V.; Muller, R. N. *Chem. Rev.* **2008**, *108*, 2064−2110.
(21) Choi, D.; Han, A.; Park, J. P.; Kim, J. K.; Lee, J. H.; Kim, T. H.; Kim, S. W. *Small* **2009**, *5*, 571−573.
(22) Han, A.; Choi, D.; Kim, T.; Lee, J. H.; Kim, J. K.; Yoon, M. J.; Choi, K. S.; Kim, S. W. *Chem. Commun.* **2009**, 6780−6782.
(23) Bae, K. H.; Kim, Y. B.; Lee, Y.; Hwang, J.; Park, H.; Park, T. G. *Bioconjugate Chem.* **2010**, *21*, 505−512.
(24) Choi, J. S.; Lee, J. H.; Shin, T. H.; Song, H. T.; Kim, E. Y.; Cheon, J. *J. Am. Chem. Soc.* **2010**, *132*, 11015−11017.
(25) Yang, H.; Zhuang, Y.; Sun, Y.; Dai, A.; Shi, X.; Wu, D.; Li, F.; Hu, H.; Yang, S. *Biomaterials* **2011**, *32*, 4584−4593.
(26) Zhou, Z.; Huang, D.; Bao, J.; Chen, Q.; Liu, G.; Chen, Z.; Chen, X.; Gao, J. *Adv. Mater.* **2012**, *24*, 6223−6228.
(27) Hu, F. Q.; Zhao, Y. S. *Nanoscale* **2012**, *4*, 6235−6243.
(28) Taboada, E.; Rodriguez, E.; Roig, A.; Oro, J.; Roch, A.; Muller, R. N. *Langmuir* **2007**, *23*, 4583−4588.
(29) Park, J. Y.; Daksha, P.; Lee, G. H.; Woo, S.; Chang, Y. M. *Nanotechnology* **2008**, *19*, 365603.
(30) Hu, F. Q.; Jia, Q. J.; Li, Y. L.; Gao, M. Y. *Nanotechnology* **2011**, *22*, 245604.
(31) Kim, B. H.; Lee, N.; Kim, H.; An, K.; Park, Y. I.; Choi, Y.; Shin, K.; Lee, Y.; Kwon, S. G.; Na, H. B.; Park, J. G.; Ahn, T. Y.; Kim, Y. W.; Moon, W. K.; Choi, S. H.; Hyeon, T. *J. Am. Chem. Soc.* **2011**, *133*, 12624−12631.
(32) Silva, A. C.; Lee, J. H.; Aoki, L.; Koretsky, A. R. *NMR Biomed.* **2004**, *17*, 532−543.
(33) Kang, Y. J.; Taton, T. A. *Angew. Chem., Int. Ed.* **2005**, *44*, 409−412.
(34) Niu, D. C.; Ma, Z.; Li, Y. S.; Shi, J. L. *J. Am. Chem. Soc.* **2010**, *132*, 15144−15147.
(35) Dong, X. P.; Shen, W. H.; Zhu, Y. F.; Xiong, L. M.; Gu, J. L.; Shi, J. L. *Microporous Mesoporous Mater.* **2005**, *81*, 235−240.
(36) Dong, X. P.; Shen, W. H.; Zhu, Y. F.; Xiong, L. M.; Shi, J. L. *Adv. Funct. Mater.* **2005**, *15*, 955−960.
(37) Chen, Y.; Chen, H. R.; Zhang, S. J.; Chen, F.; Sun, S. K.; He, Q. J.; Ma, M.; Wang, X.; Wu, H. X.; Zhang, L. X.; Zhang, L. L.; Shi, J. L. *Biomaterials* **2012**, *33*, 2388−2398.
(38) Shen, J. M.; Liu, A. D.; Tu, Y.; Wang, H.; Jiang, R. R.; Ouyang, J.; Chen, Y. *Electrochim. Acta* **2012**, *78*, 122−132.
(39) Schladt, T. D.; Graf, T.; Tremel, W. *Chem. Mater.* **2009**, *21*, 3183−3190.
(40) Taylor, K. M. L.; Kim, J. S.; Rieter, W. J.; An, H.; Lin, W. L.; Lin, W. B. *J. Am. Chem. Soc.* **2008**, *130*, 2154−2155.
(41) Seo, W. S.; Jo, H. H.; Lee, K.; Kim, B.; Oh, S. J.; Park, J. T. *Angew. Chem., Int. Ed.* **2004**, *43*, 1115−1117.
(42) Lee, E. S.; Gao, Z. G.; Bae, Y. H. *J. Controlled Release* **2008**, *132*, 164−170.
(43) Du, J. Z.; Sun, T. M.; Song, W. J.; Wu, J.; Wang, J. *Angew. Chem., Int. Ed.* **2010**, *49*, 3621−3626.
(44) Lu, J.; Ma, S. L.; Sun, J. Y.; Xia, C. C.; Liu, C.; Wang, Z. Y.; Zhao, X. N.; Gao, F. B.; Gong, Q. Y.; Song, B.; Shuai, X. T.; Ai, H.; Gu, Z. W. *Biomaterials* **2009**, *30*, 2919−2928.
(45) Ba-Ssalamah, A.; Uffmann, M.; Saini, S.; Bastati, N.; Herold, C.; Schima, W. *Eur. Radiol.* **2009**, *19*, 342−357.